

Designing tailored combinations of structural units in polymer dielectrics for high-temperature capacitive energy storage

Received: 14 December 2022

Rui Wang  ^{1,2}, Yujie Zhu ^{1,2}, Jing Fu ¹, Mingcong Yang ¹, Zhaoyu Ran ¹, Junluo Li ¹, Manxi Li ¹, Jun Hu  ¹, Jinliang He  ¹ & Qi Li  ¹ 

Accepted: 18 April 2023

Published online: 26 April 2023

 Check for updates

Many mainstream dielectric energy storage technologies in the emergent applications, such as renewable energy, electrified transportations and advanced propulsion systems, are usually required to operate under harsh-temperature conditions. However, excellent capacitive performance and thermal stability tend to be mutually exclusive in the current polymer dielectric materials and applications. Here, we report a strategy to tailor structural units for the design of high-temperature polymer dielectrics. A library of polyimide-derived polymers from diverse combinations of structural units are predicted, and 12 representative polymers are synthesized for direct experimental investigation. This study provides important insights into decisive structural factors necessary to achieve robust and stable dielectrics with high energy storage capabilities at elevated temperature. We also find that the high-temperature insulation performance would experience diminishing marginal utility as the bandgap increases beyond a critical point, which is strongly correlated to the dihedral angle between neighboring planes of conjugation in these polymers. By experimentally testing the optimized and predicted structures, an increased energy storage at temperatures up to 250 °C is observed. We discuss the possibility for this strategy to be generally applied to other polymer dielectrics to achieve further performance enhancement.

Dielectric capacitors are characteristic of ultrafast charging and discharging, establishing them as critically important energy storage elements in modern electronic devices and power systems. Polymer dielectrics have been the materials of choice for high-voltage dielectric capacitors by virtue of their high-voltage endurance and ease of processing^{1,2}. However, these organic materials are confronted with huge challenges in the emergent applications such as mainstream technologies of renewable energy, electrified transportations and advanced propulsion systems, in which electronic devices are required to operate stably under harsh-temperature conditions ranging broadly from 150 °C to over 250 °C^{3,4}. On the one hand, the commercially available capacitor films represented by biaxially oriented

polypropylene (BOPP) are designed to be of wide bandgap (E_g) and large electrical resistance, but lack the thermal stability beyond 105 °C⁵. On the other hand, although the thermal stability of heat-resistant polymers such as polyimide (PI) and fluorene polyester (FPE) far exceeds (with the glass transition temperature (T_g) over 350 °C), they contain a rich number of highly conjugated structures, which cause exponentially increased conduction loss with increasing the temperature and electric field^{6–8}. The construction of polymer-based composites has proved effective in promoting the high-temperature capacitive performance^{9–11}. Nevertheless, the performance improvement in the composites also critically depends on the hosting polymers^{12–15}. For example, the discharged energy density (U_e) of PI-

¹State Key Laboratory of Power Systems, Department of Electrical Engineering, Tsinghua University, Beijing 100084, China. ²These authors contributed equally: Rui Wang, Yujie Zhu.  e-mail: qili1020@tsinghua.edu.cn

based nanocomposite with the charge-discharge efficiency (η) $> 90\%$ is about $1\text{J}/\text{cm}^3$ at $150\text{ }^\circ\text{C}$, significantly inferior to the room-temperature energy density ($4\text{J}/\text{cm}^3$) of the commercial benchmark capacitor film¹⁶.

The high-electric-field capacitive performance and thermal stability tend to be mutually exclusive in the presently available polymer dielectrics¹⁷⁻¹⁹. This may arise from the fact that heat resistance is gained in these polymers via highly conjugated structures. Molecular modification to these polymers leads to appreciable U_e ($>2.0\text{J}/\text{cm}^3$) only below $150\text{ }^\circ\text{C}$ ^{20,21}. Very recently, a series of cyclic-olefin polymers with non-conjugated backbones and non-planar structures were synthesized, which aims at minimizing the impact of conjugation on E_g ²²⁻²⁴. The resultant polymers with concurrently high T_g ($178\text{--}244\text{ }^\circ\text{C}$) and large E_g (4.6–5 eV) show decent U_e at $150\text{ }^\circ\text{C}$ ($5.7\text{--}8.7\text{J}/\text{cm}^3$) and $200\text{ }^\circ\text{C}$ ($6.5\text{J}/\text{cm}^3$). Yet, under the temperature extreme (at $200\text{ }^\circ\text{C}$), the high U_e is achieved in these cyclic-olefin polymers at the expense of much reduced η (-80% or below), which may cause massive waste heat production and thermal runaway of devices. Moreover, the cyclic-olefin polymers are not able to operate at $250\text{ }^\circ\text{C}$ that is beyond the upper limit of T_g . Therefore, polymer dielectrics with excellent capacitive performance up to $250\text{ }^\circ\text{C}$ remain unavailable, although they are urgently desired.

We noticed that, in many of the state-of-the-art high-temperature dielectric polymers and polymer composites, hopping conduction has been revealed to be the predominant mechanism of charge transport under high-temperature and high-electric-field conditions^{9,10,20,22,25,26}. Different from some other conduction mechanisms, such as Ohmic or Poole-Frenkel emission, where electrons are mainly excited from the valence band or impurity levels to the conduction band, hopping conduction denotes the tunneling effect of electrons between adjacent charge traps in the material²⁷. Such tunneling mechanism determining the possibility of electrons to escape is not directly associated

with the bandgap of materials, but rather is relevant to the local states (the depth of trap) associated with specific material structures. Therefore, we speculate that by merely focusing on the optimization of E_g may not be able to yield the best outcome in the design of polymer dielectrics for high-temperature capacitive energy storage; Decisive structural factors in the polymer that are directly linked to the electrical performance at elevated temperatures should be figured out.

Herein, we report a tailored combination strategy for the design of polymer dielectrics towards extreme-temperature capacitive energy storage. By using a machine learning approach, we predict 110 types of PI-derived polymer structures from diverse combinations of 21 structural units that possess a wide distribution of electrical and thermal properties. We screen and synthesize 12 representative polymers all from commercial precursors in order to facilitate the large-scale production, and investigate their structures and performance systematically. By analyzing the experimental results in conjunction with computational simulations, we quantitatively determine the effect of each structural unit on the electrical and thermal properties of the resultant polymer, and unveil the key factor relevant to the capacitive performance at elevated temperatures. Based on the findings, we demonstrate that tailored combination of the structural unit can be implemented to construct the desired polymer dielectrics, leading to record energy storage performance at the temperature and electric field extremes.

Results

Machine learning for screening polymer structures

The development of polymer dielectrics for capacitive energy storage in extreme environments is usually driven by the trial-and-error method, accompanied by the shortcomings of high cost and low efficiency^{20,28-30}. Machine learning is an emergent high-throughput

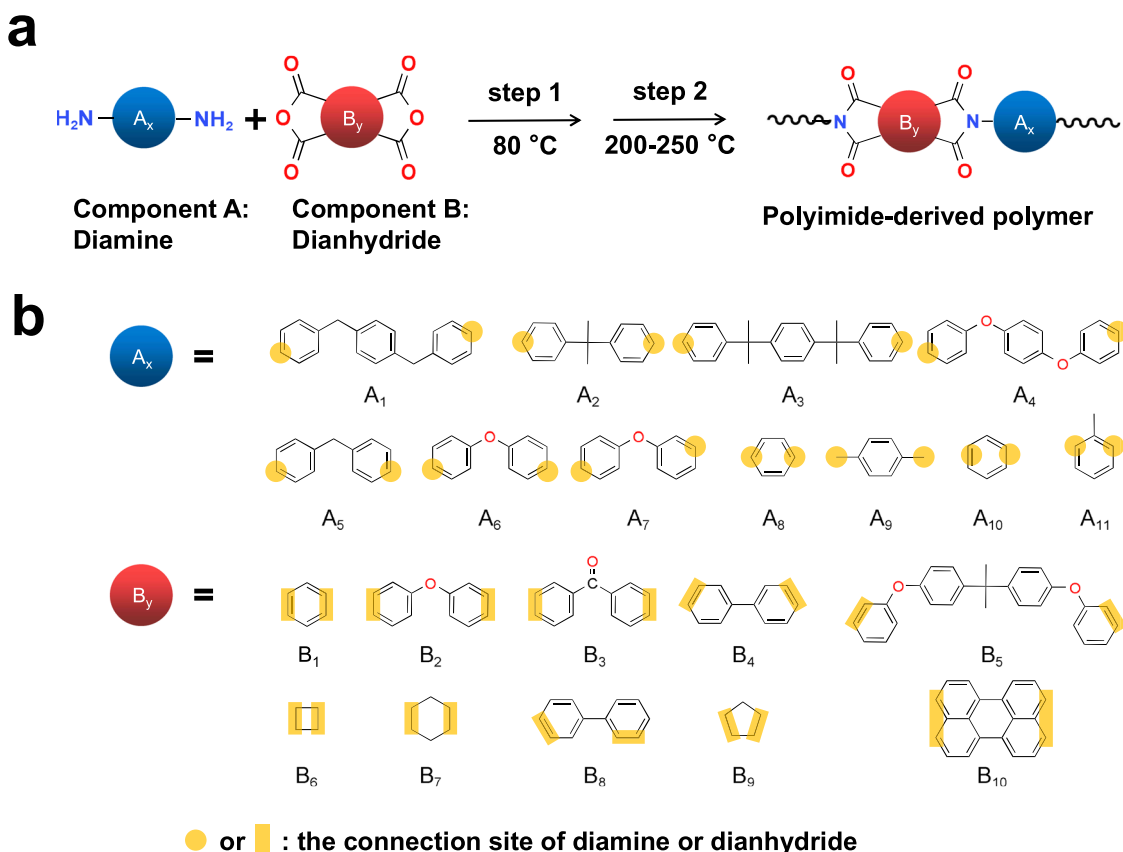


Fig. 1 | Design of polyimide-derived high-temperature polymer dielectrics.

a The schematic diagram for the synthesis route of polyimide-derived polymer dielectrics. These polymers are formed by condensation of the diamine monomer

and dianhydride monomer. **b** The chemical structures of diamine monomers (A1–A11) and dianhydride monomers (B1–B10), which are represented by the blue ball and red ball, respectively.

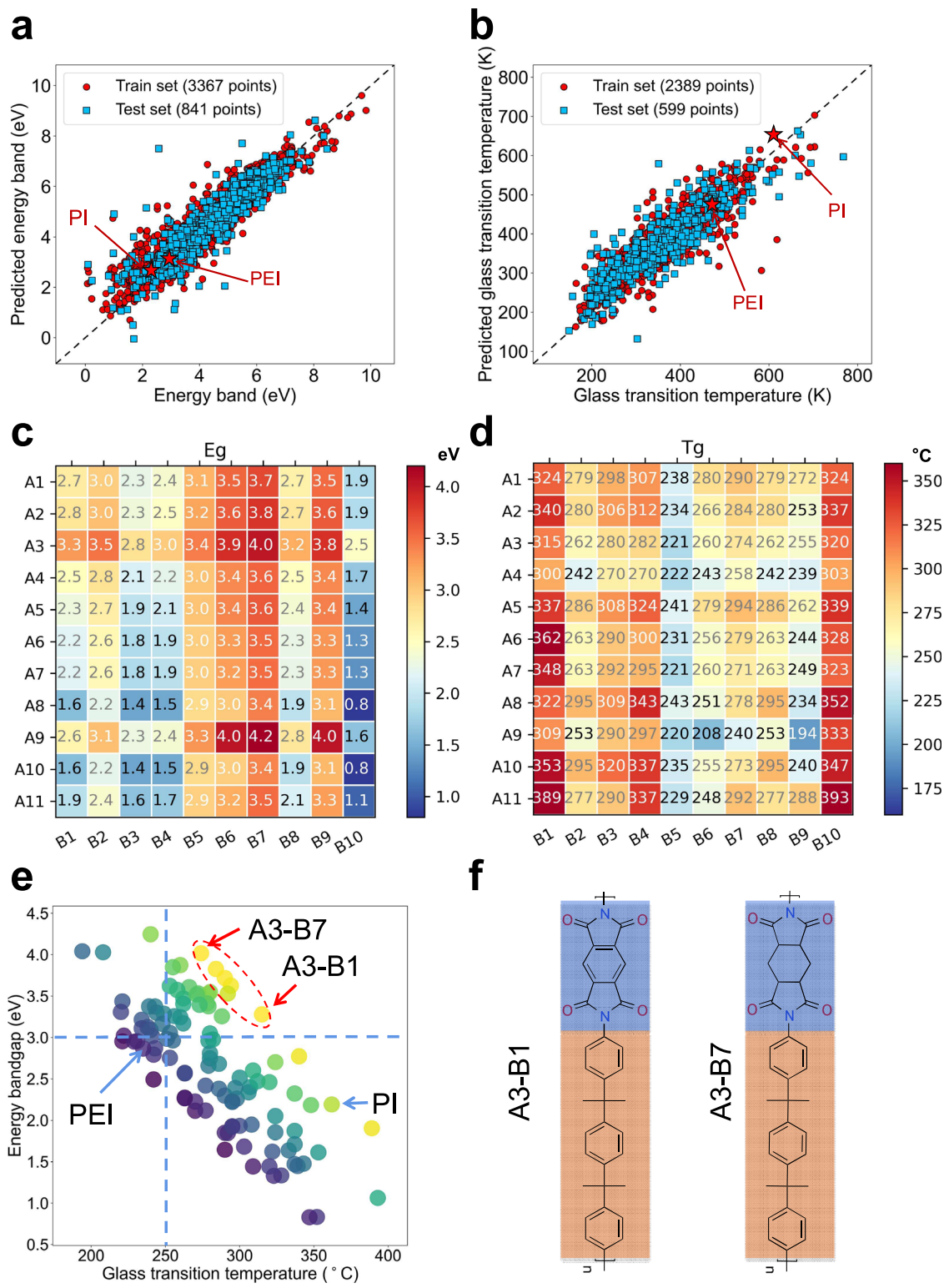


Fig. 2 | Prediction of electrical and thermal performance by machine learning. **a, b** The prediction results of the energy bandgap (E_g) and glass transition temperature (T_g) via GPR learning method. **c, d** The E_g and T_g from machine learning of the polymers composed by 11 \times 10 monomers. **e** The scatter plot of T_g versus E_g of

all the 110 possible PI-derived polymers. Two dashed lines corresponding to 3.0 eV and 250 °C are marked as guide of eyes. Coordinates for combinations of polymers are shown in Table S1 of the Supplementary Information. **f** The molecular structure of two selected PI-derived polymers with the most balanced T_g and E_g .

technology to guide the experimental design and synthesis of materials^{29–31}, which is conducive to rapid construction of “material genomes”. Here, we first utilize the machine learning approach to assist with the preliminary screening of the backbone structure of polymer dielectrics by focusing on the two attributes E_g and T_g of

materials, where E_g is usually believed to be positively related to the insulation performance³² and T_g determines the upper limit of the temperature capability²⁴. We take the PI family as the research platform, which are commonly used as heat-resistant polymers, and can be readily synthesized from the diamine and dianhydride monomers

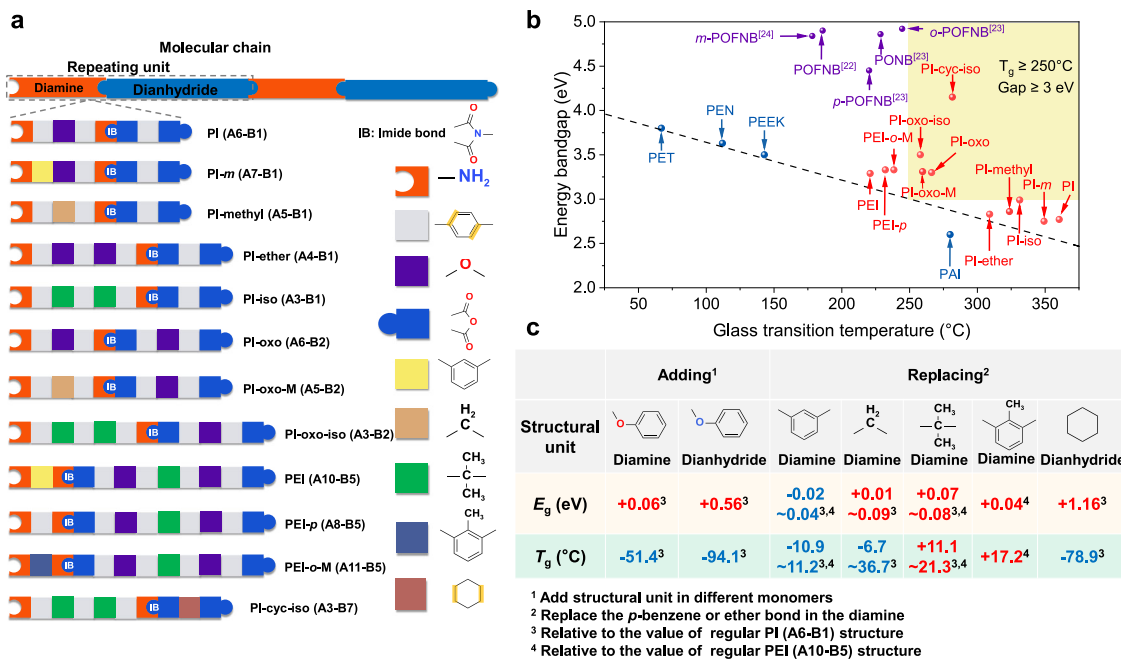


Fig. 3 | Molecular structure and property characterization. **a** Molecular structure puzzle of 12 polymers. We split the molecular structure into nine structural units, *i.e.*, amino, *p*-benzene, ether, anhydride, *m*-benzene, cyclohexane, *o*-toluene, methylene and isopropyl. **b** Comparison of electrical and thermal properties between polymers synthesized in this work, polymers reported previously and

common commercial polymers (*i.e.*, polyethylene glycol terephthalate (PET), polyethylene naphthalate (PEN), poly(ether-ether-ketone) (PEEK), and polyamide-imide (PAI)). **c** The contribution of each structural unit on the glass transition temperature and bandgap relative to the regular PI or PEI structure.

through a two-step reaction (Fig. 1a and “Methods”). For the convenience of synthesis and large-scale preparation, some uncommon or hardly synthesized monomers are avoided in our selected chemical space of PI-derived polymers for prediction. We selected 21 typical structural units to compose 11 diamine monomers (A1–A11) and 10 dianhydride (B1–B10) monomers (Fig. 1b), and predicted the respective *T_g* and *E_g* of all the possible combinations (110 PI-derived polymers in total) using the gaussian processing regression (GPR) machine learning model (Supplementary Information for details). We selected 2988 polymer samples for the *T_g* dataset and 4208 samples for *E_g* dataset, in which the data points of classic PI and polyetherimide (PEI) polymers (Supplementary Fig. S1) were repeated in the dataset for several times to improve the accuracy of the prediction (Fig. 2a, b). The *R²* parameters for *T_g* test set and *E_g* test set are 0.789 and 0.867, respectively, suggesting an accurate prediction for these two attributes.

The predicted *T_g* and *E_g* of all the 110 PI-derived polymers comprising one of the diamine monomers from A1 to A11 and one of the dianhydride monomers from B1 to B10 are shown in Fig. 2c, d, respectively, which can be further plotted in the form of *T_g* versus *E_g* (Fig. 2e). It is apparent that the two attributes (*T_g* and *E_g*) are generally inversely correlated in the PI-derived polymers, implying that the constituent structural units (A1–A11 and B1–B10) may have distinct contributions to the two attributes. To learn the exact contributions of the structural units, we first selected the two PI-derived structures with the most balanced *T_g* and *E_g* among the 110 candidates as the target polymers (Fig. 2f), which are composed of A3 and B7, and A3 and B1 (marked with red circle in Fig. 2e), respectively. We also selected 10 more structures from the 110 candidates that resemble the molecular structures of the two target polymers for comparison (Supplementary Fig. S2).

Understanding the critical role of structural units

All the 12 PI-derived polymers screened by machine learning were synthesized through the two-step reaction (Methods), and their

molecular structures were verified by Fourier transform infrared (FTIR) spectroscopy and solid-state nuclear magnetic resonance (ssNMR) spectroscopy (Supplementary Figs. S3–S15). Each of the molecular structure in the 12 polymers can be seen as the combination of various structural units, as schematically illustrated in Fig. 3a. The naming of each PI-derived polymer depends on the modification to the molecular structure of regular PI (synthesized from A6 and B1) or PEI (synthesized from A10 and B5), *e.g.*, the PI-*methyl* refers to the structure formed by replacing the ether bond in the regular PI with a methylene bond. To investigate the influence of the constituent structural units on the electrical and thermal properties of the PI-derived polymers, the 12 polymers are divided into four groups for comparison. In the first group (Group 1), including PI, PI-*m*, PEI and PEI-*p*, we mainly compare the *meta*- and *para*-substituted benzene rings in the polymers. The second group (Group 2) containing PI, PI-*methyl*, PI-ether, and PI-*iso* is to reveal the difference between ether, methylene, and isopropyl bonds on the electrical and thermal properties of polymers. The third group (Group 3), including PI, PI-*oxo*, PI-*oxo*-*M*, and PI-*oxo*-*iso*, focuses on the analysis of flexible and rigid dianhydride units. The last group (Group 4) is to understand the impact of benzene ring modification on the properties of polymers, including side group-grafting on the benzene ring (PEI-*o*-*M*) or replacing it with a saturated six-membered ring (PI-cyc-*iso*).

The *E_g* and *T_g* of the 12 PI-derived polymers were experimentally determined by ultraviolet-visible (UV-Vis) absorption spectroscopy, and differential scanning calorimetry (DSC) and dynamic mechanical analysis (DMA), respectively (Supplementary Figs. S16–S18 and Table S2). Figure 3b compares the *E_g* and *T_g* of the polymers synthesized in this work with those of commercial polymers. The experimentally determined *E_g* and *T_g* are comparable to those predicted by machine learning (Supplementary Fig. S19), demonstrating the reliability of machine learning in preliminary screening of polymer structures. In the analysis of Group 1, we found that while the *T_g* values of polymers with *p*-benzene structural unit are significantly larger compared to those containing the *m*-benzene structural unit (*e.g.*, 360.5 °C of PI

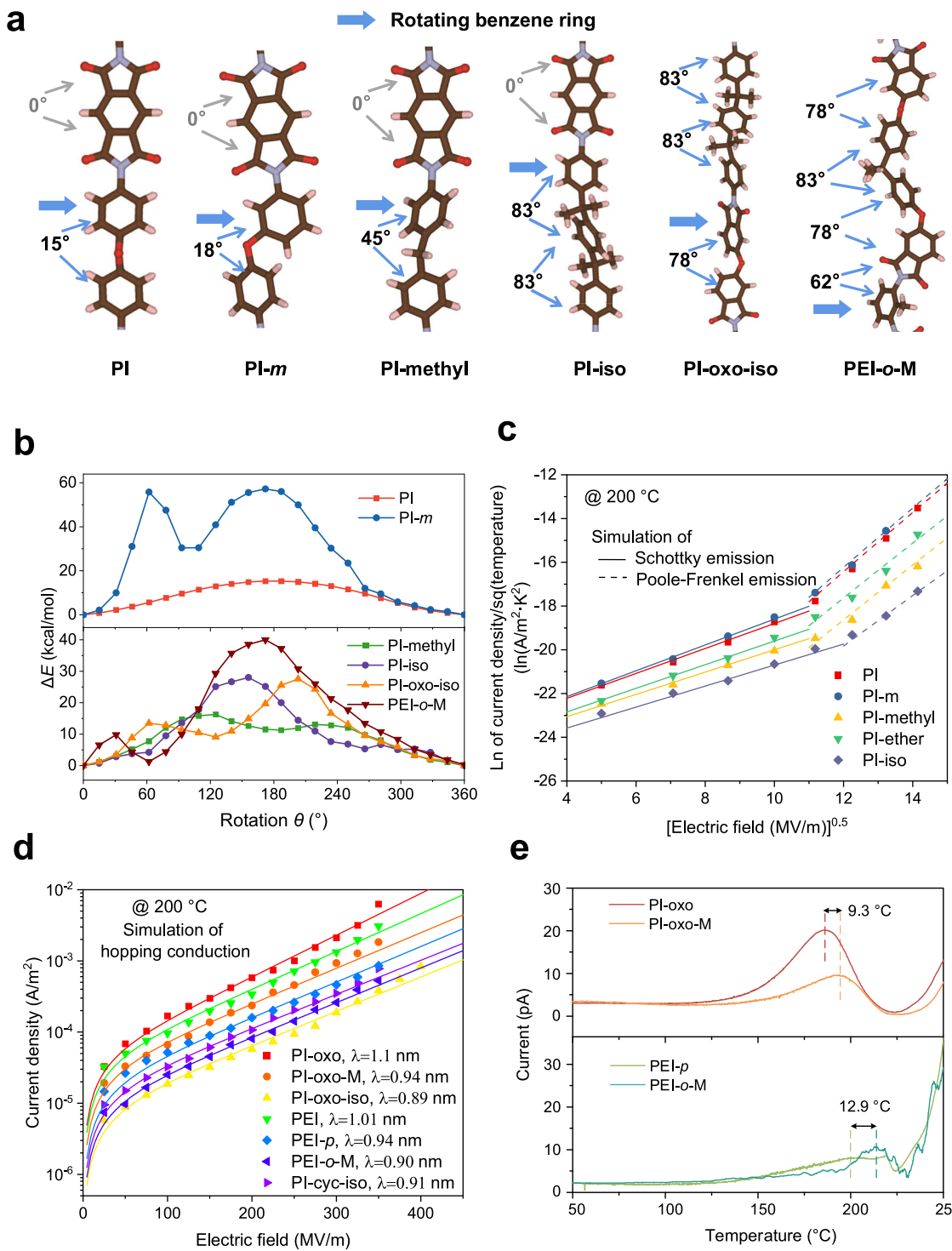


Fig. 4 | Charge transport mechanism. **a** Schematic diagram of six polymer chains at the lowest energy. **b** The rotational energy barrier of benzene ring as a function of rotation angle. **c** Current density of the PI-derived polymers synthesized from pyromellitic dianhydride as a function of electric field at 200 °C. **d** Current density

of PI-derived polymers synthesized from long-chain dianhydride monomers as a function of electric field at 200 °C. **e** Thermally stimulated depolarization current of two groups of polymers with the same E_g .

versus 349.3 °C of PI-*m*, and 232.2 °C of PEI-*p* versus 221.3 °C of PEI, their E_g values are quite similar (e.g., 2.77 eV of PI versus 2.75 eV of PI-*m*, and 3.33 eV of PEI-*p* versus 3.29 eV of PEI). The characterization of Group 2 revealed that the isopropyl structural unit in the diamine monomer offers slightly improved E_g and T_g over the ether unit, e.g., E_g and T_g of PI-iso increased by 0.16 eV and 22.2 °C, respectively, relative to PI-ether. By contrast, as suggested by the comparison in Group 3, the insertion of ether structural units into the dianhydride monomers

resulted in dramatic changes of E_g (raised by 0.53 eV) and T_g (declined by 94.1 °C). The comparison in Group 4 unveiled that the side group connected on the benzene ring is conducive to the concurrent promotion of T_g and E_g (raised by 17.2 °C and 0.04 eV, respectively), and that the substitution of benzene ring with cyclohexane structure results in significantly increased E_g (raised by 1.16 eV) and decreased T_g (declined by 49.7 °C). Based on the afore-mentioned experimental results, we are able to extract the exact impact of adding (or replacing)

each structural unit on the E_g and T_g values of the PI-derived polymers, which are quantitatively benchmarked to the regular PI (*i.e.*, A6-B1) or PEI (*i.e.*, A10-B5) (Fig. 3c). For instance, the quantitative impact of adding an ether bond on the E_g and T_g values can be obtained by subtracting the data of PI-ether and PI. Similarly, by subtracting the data of PI-iso and that of PI-ether then dividing them by 2, we can get the quantitative impact of isopropyl relative to ether bond on the E_g and T_g values.

Decisive structural factor to the high-temperature insulation performance

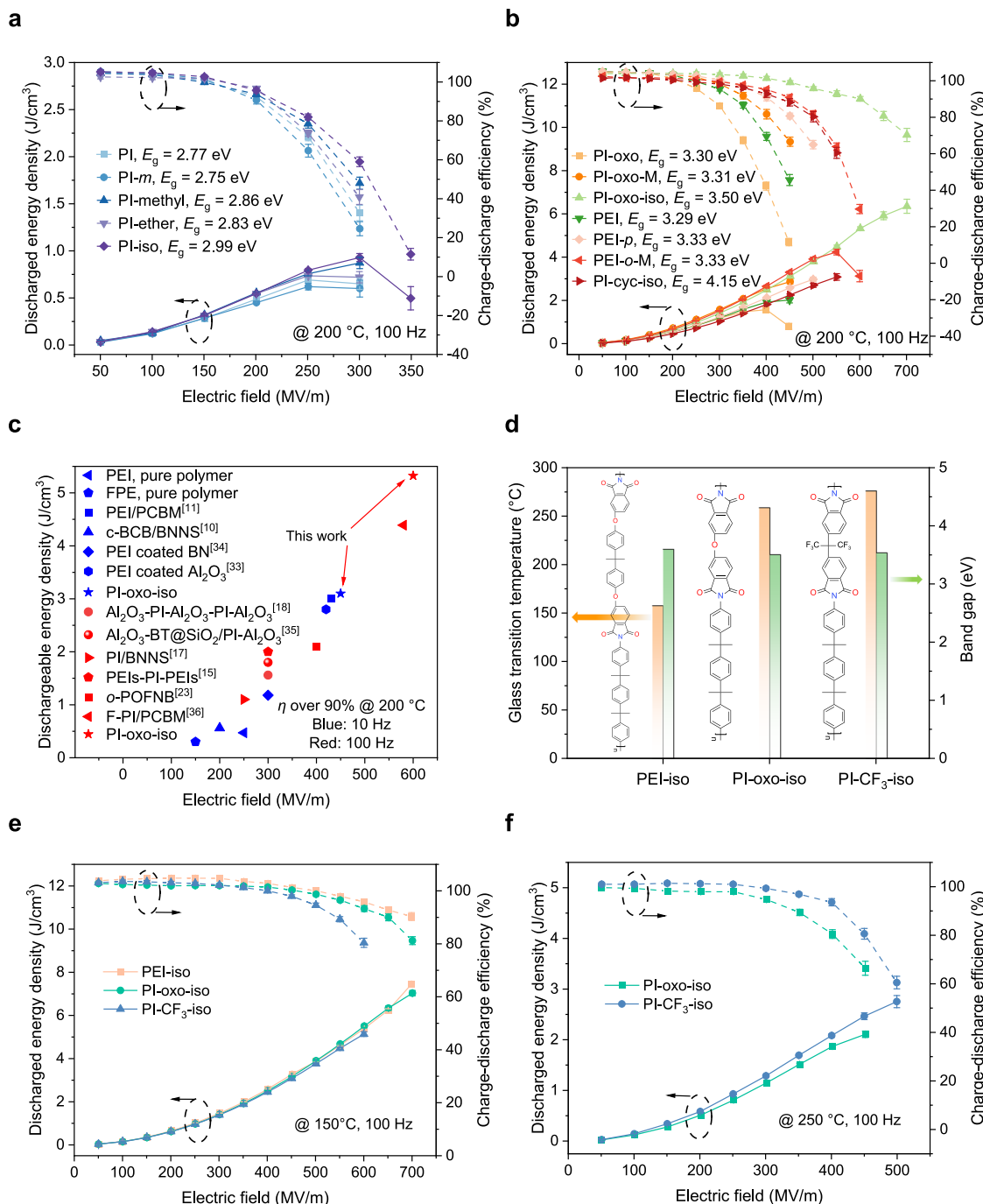
According to the prior notion^{22–24}, a larger E_g of the polymer dielectric would result in greater high-temperature insulation and capacitive performance. Unexpectedly, we found that under high temperature (200 °C) and high-electric field (up to 400 MV/m) conditions, the measured leakage current density (Supplementary Fig. S25) of the PI-derived polymers (with the T_g values all above 200 °C) does not comply with the trend of their respective E_g values. For example, PI-cyc-iso with a high E_g of 4.15 eV exhibits higher leakage current density (poorer insulation performance) than PI-oxo-iso with a lower E_g of 3.5 eV. Therefore, we speculate that there are other factors affecting the high-temperature insulation performance of polymer dielectrics. We thus simulated the conjugation state of various PI-derived polymers in the lowest energy state through the molecular dynamics (MD) simulation (Fig. 4a), and determined the interaction between adjacent conjugated planes by comparing the rotational energy barrier obtained from rotating a ring structure around single bond (Fig. 4b). The impact of structural units on the interaction can be understood from two aspects. On the one hand, the conjugated planes in the molecular structure of PI and PI-*m* tend to be nearly coplanar (with the dihedral angle between adjacent benzene rings in the diamine $<20^\circ$, Fig. 4a), and the rotational energy barrier with *p*-benzene structure (*i.e.*, regular PI) is significantly lower than that with *m*-benzene structure (16.3 kcal/mol versus 56.5 kcal/mol, Fig. 4b). In this case, the regular PI is less stable in the nearly coplanar state, and thereby is characteristic of weakened interaction with respect to the PI-*m*. On the other hand, the *ortho*-substituted methyl on the benzene ring, the ether bond in the dianhydride, and the isopropyl/methylene in the diamine all render the dihedral angle between adjacent benzene rings quite large ($\geq 45^\circ$, Fig. 4a). In this case, the molecular structure with higher rotational energy barrier is more difficult to approach the coplanar state, giving rise to a stabilized state of weak interaction.

We found that the energy bandgap of the PI-derived polymers is not coupled with the dihedral angle between adjacent conjugated planes, as indicated by the density functional theory (DFT) computations of E_g in the process that we progressively rotate one specific benzene ring in the polymer (Supplementary Fig. S27). To correlate the interaction between adjacent conjugated planes with the high-temperature insulation performance, we define the average dihedral angle (θ) as the average measure of all the dihedral angles of adjacent conjugated planes in the diamine and dianhydride in one repeating unit of the polymer. For instance, in the PI-oxo-iso, there are three such dihedral angles with the measures of angle being 83°, 83° and 78°, and θ is calculated as $(83^\circ + 83^\circ + 78^\circ)/3 = 81.3^\circ$. Interestingly, it was unveiled that the trends of leakage current density (Supplementary Fig. S25) of the PI-derived polymers with E_g above 3.3 eV match well with that of θ (Supplementary Tab. S3). The above analysis suggests that the interaction between adjacent conjugated rings is a decisive factor affecting the high-temperature insulation performance.

To understand why the interaction between adjacent conjugated rings plays a critical role, we investigated the conduction mechanisms of the materials. Since the leakage current of the material increases exponentially with the temperature, it is more meaningful to explore the conduction mechanism at higher temperature (*e.g.*, at 200 °C). It was revealed that, the pattern in which the leakage current density

measured under high temperature and high-electric field varies with the electric field is different between the polymers with E_g above 3.3 eV and those with E_g below 3.0 eV, clearly indicative of two distinct conduction mechanisms. To be specific, in the PI-derived polymers with rigid dianhydride (with $E_g < 3.0$ eV), the fitting of the leakage current density versus electric field curve measured under 200 °C shows the transition from Schottky injection to Poole-Frenkel emission with the increase of electric field (Fig. 4c, and Supplementary Fig. S26a); By contrast, the fitting in the polymers with broken conjugated structure of dianhydride (with $E_g > 3.3$ eV) conforms to the hopping conduction within the measured range of applied electric field (Fig. 4d, and Supplementary Fig. S26b). These results, along with the fundamental difference between Schottky injection/Poole-Frenkel emission and hopping conduction suggest that, in the case of polymers possessing relatively low E_g (< 3.0 eV), electrons can gain enough energy under high temperature and high-electric field to be injected from the electrode into the dielectric or to be excited from the valence band to the conduction band, whereas in the case of polymers with relatively high E_g (> 3.3 eV), they are more likely to be conducted through the tunneling effect between adjacent traps. Moreover, in the PI-derived polymers featuring hopping conduction ($E_g > 3.3$ eV), the energy level of charge traps was found to be irrelevant to the E_g value, as confirmed by the result of thermally stimulated depolarization current (TSDC, Fig. 4e) and calculated hopping distance (Supplementary Tab. S3). For example, while the depolarization current peak corresponding to the detrapping of charge carriers in PI-oxo is located at a lower temperature than that of PI-oxo-M (182.8 °C versus 192.1 °C, characteristic of a smaller trap depth in the former), these two polymers have exactly the same E_g value ($E_g = 3.3$ eV). This is also true in the comparison between PEI-*p* and PEI-*o*-M, whose depolarization current peaks are centered at 200.3 °C and 214.1 °C, respectively. Strikingly, we found that the trap depth in the PI-derived polymers is positively related to θ (Supplementary Tab. S3), meaning that a greater number of large dihedral angles dihedral angles render the tunneling of electrons more difficult. This is supported by the fact that the leakage current density shares the same trend to that of θ . Summarizing all the results discussed in this section, a new insight can be gained, which challenges the conventional notion and might be critically important for the design of high-temperature polymer dielectrics for energy storage, *i.e.*, the high-temperature insulation performance may experience diminishing marginal utility as the bandgap increases beyond a critical point (about 3.3 eV in the PI-derived polymers) where the predominant conduction mechanism changes from Poole-Frenkel emission to hopping, and then the dihedral angle between adjacent plane of conjugation would become the decisive factor.

In addition, we evaluated the breakdown strength of PI-derived polymers at 150 and 200 °C, and found that the trend of leakage current is consistent with the breakdown strength (Supplementary Fig. S29), suggesting that electrical breakdown is the main mechanism causing the failure of PI-derived polymers. Subsequently, we characterized the dielectric properties of PI-derived polymers. Except that the dielectric constant of PI-cyc-iso decreases to 2.72 due to the replacement of benzene ring with cyclohexane, the dielectric constant of other polymers at high temperatures is similar (ranging from 3 to 3.4) owing to the fact that the structural unit all exhibit weak polarity (Supplementary Fig. S30). However, the dielectric dissipation shows frequency and temperature dependence, *e.g.*, the dielectric loss of PI-derived polymers with $E_g < 3.0$ eV increases significantly at low frequencies (10^2 – 10^3), which can be attributed to the increase of the conduction loss. To further clarify the temperature stability of the dielectric properties of PI-oxo-iso, we evaluated the temperature-dependent dielectric spectrum of PI-oxo-iso ranging from 30 to 250 °C at 1000 Hz, and compared it with typical polymers (PI and PEI). As show in Supplementary Fig. S31, it was proved that the dielectric properties of PEI and PI-oxo-iso remain stable below the glass



transition temperature, while PI presents a slightly decreased dielectric constant with the increase of temperature.

Capacitive energy storage performance

To examine the new understandings, we next studied the energy storage performance of the PI-derived polymers by measuring the unipolar electric displacement-electric field (D - E) loops at high temperature (Fig. 5, and Supplementary Figs. S33–S44). It is apparent that the high-temperature energy storage performance (U_e and η) of

the polymers with relatively low E_g (<3.0 eV) complies with the trend of E_g . As E_g increases from 2.75 to 2.99 eV, the U_e and η of polymers gradually increase from 0.6 J/cm³ and 25% to 0.9 J/cm³ and 59%, respectively, which can be attributed to the dependence of Schottky injection barrier and Poole-Frenkel emission activation energy on the E_g (Fig. 5a). By sharp contrast, in the polymers with relatively high E_g (>3.3 eV), in which hopping conduction is the predominant mechanism, the high-temperature energy storage performance is no longer in accordance with the pattern of E_g (Fig. 5b). For example, while the E_g of

PI-cyc-iso is higher than that of PI-oxo-iso (4.15 eV versus 3.5 eV), the U_e of the former is much inferior to that of the latter at 150 °C (Supplementary Fig. S45) and 200 °C (Fig. 5b), which corroborates that by merely focusing on the optimization of E_g may not be able to yield the best high-temperature capacitive performance. Furthermore, at 200 °C, the polymer with greater θ exhibits higher U_e , e.g., PI-oxo-iso, with the largest θ (81.3°) of all the samples, possesses the highest U_e (6.4 J/cm³). This result solidifies the decisive role of the dihedral angle between adjacent conjugated planes in the design of PI-derived high-temperature dielectrics.

In addition to U_e , the maximum discharged energy density above 90% charge-discharge efficiency (U_{e90}) is even more important for the high-temperature energy storage^{9,11}. This is because an energy density achieved at low efficiencies (-80% or lower) is inevitably accompanied with massive heat dissipation, and may cause thermal runaway of the device under high temperature that is close to the thermal limit of material. We compared the U_{e90} of PI-oxo-iso with the previous best results reported in the literature (Fig. 5c, Supplementary Tab. S4). Impressively, the U_{e90} of the polymer reported in this work is as high as 5.3 J/cm³, surpassing all the existing pure polymers and their composites^{10,11,15,17,18,23,33–36}. Note that, although the previous best high-temperature polymer dielectric (cyclic-olefin polymer)²³ delivers a high U_e (6.5 J/cm³) at 200 °C that is comparable to the PI-oxo-iso, its U_{e90} is merely around 2 J/cm³, suggesting that the PI-oxo-iso would significantly outperform the cyclic-olefin polymer at the temperature and electric field extremes. Besides, the PI-derived polymers reported in this work are all prepared with mature synthetic approach using commercial precursors, which facilitates large-scale production.

We further characterized the quality of the high-performance dielectric film (PI-oxo-iso) to evaluate its suitability for industrial production and application. The results of atomic force microscopy (AFM) and scanning electron microscopy (SEM) show that the PI-oxo-iso film is of a small surface roughness ($R_a = 0.22$ nm) without perceptible defect (Supplementary Figs. S47 and S48). The homogeneity of the film was investigated on a 20 × 20 cm² area by measuring the high-temperature capacitive performance, which is overall stable in different regions (Supplementary Fig. S49). The ability to form high-quality films was also confirmed in different film thicknesses with various electrode areas by testing the breakdown strength (Supplementary Figs. S50 and S51). In addition, the energy storage performance of the film exhibits decent cyclic and temperature stability (Supplementary Figs. S52 and S53), both of which are important for capacitor application.

With the specific function of each structural unit fully understood, we are able to customize polymer dielectrics with the optimal capacitive performance at different temperature conditions. The design concept is based on three primary principles: Firstly, E_g should be higher than 3.3 eV to ensure the hopping conduction; Secondly, T_g needs to be more than 10 °C higher than the target operating temperature to secure the thermal stability; Thirdly, as many as possible large angle conjugated rings should be added to the polymer chain to increase the trap depth. Based on these principles, we implemented tailored combination of the structural units, and synthesized 2 more polymers, i.e., PEI-iso and PI-CF₃-iso designed for the applications at 150 °C and 250 °C, respectively (Fig. 5d, Supplementary Figs. S54–S56 for details). PEI-iso was obtained by adding ether and isopropyl structural units in the dianhydride of PI-oxo-iso, which inserted two large dihedral angles to the molecule and reduced the T_g value by 81.5–91.7 °C relative to the PI-oxo-iso (therefore the T_g of PEI-iso should be in the range of 166.5–176.7 °C). PI-CF₃-iso was designed by replacing the ether unit in the dianhydride of PI-oxo-iso with hexafluoroisopropylidene (similar to isopropyl, since the dianhydride containing hexafluoroisopropylidene is commercially available) to increase the T_g , and the T_g of PI-CF₃-iso is predicted to be in the range of 269.3–279.5 °C. The experimental results show that the E_g values of

PEI-iso and PI-CF₃-iso are 3.59 eV and 3.53 eV (Fig. 5d, Supplementary Fig. S58), respectively, and their T_g values are 167.4 °C and 275.5 °C (Fig. 5d, Supplementary Figs. S59 and S60), respectively, exhibiting good agreement with the values predicted by the tailored combination. Outstandingly, PEI-iso shows the highest U_{e90} (7.5 J/cm³) at 150 °C among all the synthesized polymers in this study and other polymers and composites reported previously (Fig. 5e, Supplementary Fig. S63). More strikingly, PI-CF₃-iso possesses unprecedented energy storage performance at 250 °C (U_{e90} of 2.1 J/cm³) (Fig. 5f, Supplementary Figs. S64 and S65), which is over an order of magnitude larger than that of the best polymer and polymer composite (U_{e90} less than 0.2 J/cm³) reported in the literature¹⁰. The result from mechanical test shows that all the high-performance polymers including PI-oxo-iso, PEI-iso and PI-CF₃-iso have comparable mechanical strength to the regular PEI (Supplementary Figs. S23 and S57), which has been proved to be able to form thin capacitor films.

Discussion

A tailored combination of structural units is demonstrated for the design of high-temperature polymer dielectrics. By using machine learning, polymer structures with a broad range of electrical and thermal properties are screened out, which enables grouped comparisons and quantitative description of the impact of each structural unit on the E_g and T_g of polymers. Besides, the prediction by machine learning also offers plentiful enough polymer structures with high E_g and high T_g . In-depth experimental investigation on the electrical properties reveal that the high-temperature insulation performance would experience diminishing marginal utility as the bandgap increases beyond a critical point (about 3.3 eV) in these polymers, where the predominant conduction mechanism changes from Poole-Frenkel emission to hopping. MD and DFT simulations suggest that dihedral angles between adjacent conjugated planes in the molecule play a decisive role in determining the extreme-temperature capacitive performance. This is strikingly different from the prior notion that optimization of E_g would yield the best capacitive performance at high temperature. Based on these understandings, three different polymer structures are designed via the tailored combination of structural units, for operation under 150, 200, and 250 °C, respectively, all exhibiting record discharged energy densities above 90% efficiency under the respective temperature conditions (7.5, 5.3, and 2.1 J/cm³). The strategy reported in this work may offer new possibilities to resolve the challenging dilemma of achieving excellent capacitive performance at the temperature and electric field extremes.

Methods

Materials

Pyromellitic dianhydride, 4,4'-diaminodiphenyl ether, *m*-phenylenediamine, 3,4'-diaminodiphenyl ether, *p*-phenylenediamine, 5,5'-(propane-2,2-diylbis(4,1-phenylene))bis(oxy)bis(isobenzofuran-1,3-dione), and 4,4'-diaminodiphenylmethane were purchased from Sigma-Aldrich. α,α' -Bis(4-aminophenyl)-1,4-diisopropylbenzene, 4-bis(4-aminophenoxy)-benzene, 4,4'-(hexafluoroisopropylidene)diphthalic anhydride and 4,4'-oxydiphthalic anhydride were purchased from TCI. 2-Methyl-*m*-phenylenediamine and 1,2,4,5-cyclohexanetracarboxylic dianhydride were provided by Anhui Zesheng Technology Co., Ltd.

Synthesis of polymers

All polymers are synthesized by solution method. First, a certain mass of dianhydride monomer was added to 10 mL of *N*-methyl-2-pyrrolidinone (NMP) solution. Then, an equal molar amount of diamine monomer was added to the mixed solution, followed by stirring at 80 °C for 12 h to ensure that the diamine and the dianhydride monomer reacted to form a poly(amic acid). Due to the different molecular weights of dianhydride and diamine monomers, the total

monomer mass in the various solutions we prepared here was always kept within the range of 300–400 mg, and the specific amount of monomers in all polymer synthesis processes is shown in Table S5 (Supplementary Information). Afterwards the reacted solution was cast on a pre-cleaned glass plate and dried at 80 °C for 12 h. To make the poly(amic acid) undergo the imidization reaction, we need to conduct additional high-temperature treatment on the sample. The polymers were heat-treated in an oven by a gradient heating method, kept at 100, 150, 200, and 250 °C in sequence for 1 h. After naturally cooling to room temperature, the film was peeled off from the glass substrate in water, and vacuum-dried in a 100 °C oven to remove residual moisture.

Characterization

Solid-state NMR carbon spectra were recorded on a JNM-ECZ600R spectrometer. In the ^{13}C NMR test, the resonance frequency was 150 MHz, the relaxation delay was 5 s, the linewidth factor was 80 Hz, the mas frequency was 12 kHz, and the contact time was 2 ms. Fourier transform infrared spectra (FTIR) were recorded on a Thermo Scientific Nicolet iS10 spectrometer using the attenuated total reflectance (ATR) mode. Differential scanning calorimetry (DSC) was carried out by a DSC system (TA Instrument Q100, USA) from 30 °C to 400 °C at 10 °C/min. Dynamic mechanical analysis (DMA) was performed by a TA Instruments DMAQ800 at a heating rate of 5 °C/min. UV–vis absorption spectra were measured by a Hitachi U-3010 spectrophotometer ranging from 200 to 700 nm with wavelength accuracy of ± 0.3 nm. Thermogravimetric analysis (TGA) was performed by a Thermo-gravimetry (TA Instruments Q5000IR, USA) ranging from 30 °C to 800 °C at 10 °C/min under a nitrogen atmosphere. Atomic force microscopy (AFM) for surface morphology were obtained by a Bruker Dimension Icon atomic force microscope in tapping mode. Gel permeation chromatography (GPC) was used on a high-performance liquid chromatography (Waters E2695 Alliance) to obtain molecular weights, where the solvent was DMA. In the mechanical property test, the sample was cut into a long strip of 10 mm wide and 40 mm long (the effective length of all samples is 30 mm), and stretched at a rate of 2 mm/min until it breaks to obtain the stress-strain curve. The slope of the tangent under 5% strain is defined as Young's modulus. Scanning electron microscopy (SEM) were conducted on a ZEISS MERLIN Compact field emission electron microscope. Before measuring the electrical and dielectric properties, aluminum electrodes were evaporated on both sides of the film using a BENCH TOP TURBO evaporative coating instrument from Denton Vacuum. A Novocontrol Concept 80 dielectric spectroscopy meter equipped with a Quatro-Cryosystem temperature control system was used for obtaining dielectric constant and dissipation factor, the electrode diameter used in this test was 10 mm. Leakage currents were performed on a Keithley 6517B amperemeter, and the voltage and temperature were controlled by a Stanford PS350 voltage source and an oven, respectively. Dielectric breakdown strength was recorded on a TREK 610C amplifier at a voltage rise rate of 500 V/s, 15 data were obtained for each sample and analyzed by the two-parameter Weibull statistic. In the dielectric breakdown strength and leakage current tests, the electrode diameter of the sample was 2 mm. The electric displacement–electric field (D – E) loops were recorded on a modified Sawyer-Tower circuit under a unipolar wave at the frequency of 10/100 Hz, and the electrode diameter used in this test was 3 mm. In the breakdown strength and D – E loops tests, the testing samples were soaked in dimethylsiloxane, and the temperature of silicone oil was controlled by a hot plate equipped with a temperature sensor. The thermally stimulated discharge current (TSDC) tests were measured by a Keithley 6517B amperemeter equipped with a Quatro-Cryosystem temperature control system. First, all samples were polarized under 50 MV/m DC poling electric field for 30 min at 200 °C, then quickly cooled to 30 °C with the electric field remaining 50 MV/m. Finally, removed the electric field and short-

circuit the sample after holding at 30 °C for 10 min, heated the sample to 300 °C at a heating rate of 3 °C/min, and recorded the current at each temperature point.

Machine learning

The T_g and E_g prediction model for PI-derived system is trained by polymers from linear polymer chemical space, which is collected from PolyInfo dataset³⁷ and Kahazana dataset³⁸. Particularly, Due to fact that the calculated E_g values are usually lower than the experimental ones, we replaced some E_g values of PI-derived polymers in the training dataset with experimental data from previous literature^{11,39} to improve the accuracy of prediction. We also took the K-fold ($k=5$) method, where all the data except for those of the PI-derived polymers in the training dataset are divided into five parts and the data of the PI-derived polymers are trained in every part. The dataset has been plotted in Fig. S1 where the PI-derived polymers are highlighted. The T_g dataset contains 2988 samples collected from PolyInfo dataset, and the E_g dataset contains 4208 samples collected from Kahazana dataset. The datasets contain 7 elements, i.e., C, H, O, N, S, F, Cl. The fingerprint contains two parts.

One is collected from the traditional molecular fingerprint, which represents the content of fragment inside the monomer unit. The fragment is collected from MACCS public keys and the basic groups form dataset polymers. Moreover, different molecular fingerprint features are also added, like BalabanJ, TPSA, etc., which can be achieved by the RDKit python package. The other part contains the unique feature of polymer monomer unit, compared with the molecular fingerprint, like the length of the main chain. Overall, 781 dimension fingerprint has been generated for prediction. The machine learning method for prediction is the Gaussian processing regression (GPR), where rational quadratic (RQ) kernel is introduced for selection combined with the fingerprint engineering method (RFE). Considering that the minor difference between the predicted results and the experimental results is acceptable (Fig. S19), the machine learning method Gaussian processing regression (GPR) model is applied rather than other machine learning methods (neural network, random forest, decision tree, etc.). In the prediction, 80% of the dataset are divided into the training set and 20% are set to the test set. In the training set, k-fold cross validation ($k=5$) are introduced for increasing the training set scale.

Density functional theory methods

The density functional theory (DFT) has been performed in the software VASP, where the self-consistence calculation tends to underestimate bandgap E_g of dielectric polymer by 30% or more^{40–42}. Thus, Heyd–Scuseria–Ernzerhof (HSE06) hybrid function is employed in the bandgap calculation of the single PI polymer chain⁴³. However, the bandgap values of polymers are still underestimated. The results are only used for qualitative analysis here. In addition, the rotation energy is also calculated via this method.

Data availability

The data that support the findings of this study are available from the authors on request.

Code availability

The code that supports the findings of this study is available from the authors on request.

References

1. Sarjeant, W. J., Clelland, I. W. & Price, R. A. Capacitive components for power electronics. *Proc. IEEE* **89**, 846–855 (2001).
2. Tan, Q., Irwin, P. & Cao, Y. Advanced dielectrics for capacitors. *IEEE Trans. Fund. Mater.* **126**, 1152–1159 (2006).
3. Jeff, W. & Castro, G. High-temperature electronics pose design and reliability challenges. *Analog Dialogue* **46**, 3–9 (2012).

4. Buttay, C. et al. State of the art of high temperature power electronics. *Mater. Sci. Eng. B* **176**, 283–288 (2011).
5. Tan, D. et al. High-temperature capacitor polymer films. *J. Electron. Mater.* **43**, 4569–4575 (2014).
6. Li, Q. et al. High-temperature dielectric materials for electrical energy storage. *Annu. Rev. Mater. Res.* **48**, 219–243 (2018).
7. Ho, J. S. & Greenbaum, S. G. Polymer capacitor dielectrics for high temperature applications. *ACS Appl. Mater. Inter.* **10**, 29189–29218 (2018).
8. Liu, X. J. et al. High-temperature polyimide dielectric materials for energy storage: theory, design, preparation and properties. *Energy Environ. Sci.* **15**, 56–81 (2022).
9. Li, H. et al. Scalable polymer nanocomposites with record high-temperature capacitive performance enabled by rationally designed nanostructured inorganic fillers. *Adv. Mater.* **31**, 1900875 (2019).
10. Li, Q. et al. Flexible high-temperature dielectric materials from polymer nanocomposites. *Nature* **523**, 576–579 (2015).
11. Yuan, C. et al. Polymer/molecular semiconductor all-organic composites for high-temperature dielectric energy storage. *Nat. Commun.* **11**, 3919 (2020).
12. Marwat, M. A. et al. Ultrahigh energy density and thermal stability in sandwich-structured nanocomposites with dopamine@Ag@Ba-TiO₃. *Energy Storage Mater.* **31**, 492–504 (2020).
13. Ren, W. B. et al. High-temperature electrical energy storage performances of dipolar glass polymer nanocomposites filled with trace ultrafine nanoparticles. *Chem. Eng. J.* **420**, 127614 (2021).
14. Miao, W. J. et al. Enhancement thermal stability of polyetherimide-based nanocomposites for applications in energy storage. *Compos. Sci. Technol.* **201**, 108501 (2021).
15. Niu, Y. J. et al. Significantly enhancing the discharge efficiency of sandwich-structured polymer dielectrics at elevated temperature by building carrier blocking interface. *Nano Energy* **97**, 107215 (2022).
16. Ai, D. et al. Tuning nanofillers in in situ prepared polyimide nanocomposites for high-temperature capacitive energy storage. *Adv. Energy Mater.* **10**, 1903881 (2020).
17. Zhang, K. Y. et al. Improving high-temperature energy storage performance of PI dielectric capacitor films through boron nitride interlayer. *Adv. Composit. Hybrid Mater.* **5**, 238–249 (2022).
18. Dong, J. F. et al. A facile in situ surface-functionalization approach to scalable laminated high-temperature polymer dielectrics with ultra-high capacitive performance. *Adv. Funct. Mater.* **31**, 2102644 (2021).
19. Li, H. et al. Dielectric polymers for high-temperature capacitive energy storage. *Chem. Soc. Rev.* **50**, 6369–6400 (2021).
20. Li, H. et al. Crosslinked fluoropolymers exhibiting superior high-temperature energy density and charge-discharge efficiency. *Energy Environ. Sci.* **13**, 1279–1286 (2020).
21. Cheng, Z. X. et al. Aromatic poly(arylene ether urea) with high dipole moment for high thermal stability and high energy density capacitors. *Appl. Phys. Lett.* **106**, 202902 (2015).
22. Wu, C. et al. Flexible temperature-invariant polymer dielectrics with large bandgap. *Adv. Mater.* **32**, 2000499 (2020).
23. Deshmukh, A. A. et al. Flexible polyolefin dielectric by strategic design of organic modules for harsh condition electrification. *Energy Environ. Sci.* **15**, 1307–1314 (2022).
24. Wu, C. et al. Flexible cyclic-olefin with enhanced dipolar relaxation for harsh condition electrification. *P. Natl. Acad. Sci. USA* **118**, e2115367118 (2021).
25. Ren, L. L. et al. High-temperature high-energy-density dielectric polymer nanocomposites utilizing inorganic core-shell nanostructured nanofillers. *Adv. Energy Mater.* **11**, 2101297 (2021).
26. Li, Q. et al. Sandwich-structured polymer nanocomposites with high energy density and great charge-discharge efficiency at elevated temperatures. *Proc. Natl Acad. Sci. USA* **113**, 9995–10000 (2016).
27. Chiu, F. C. A review on conduction mechanisms in dielectric films. *Adv. Mater. Sci. Eng.* **2014**, 578168 (2014).
28. Wang, Y. F. et al. Polyamideimide dielectric with montmorillonite nanosheets coating for high-temperature energy storage. *Chem. Eng. J.* **437**, 135430 (2022).
29. Vinit, S. et al. Rational design of all organic polymer dielectrics. *Nat. Commun.* **5**, 1–8 (2014).
30. Shen, Z. H. et al. Phase-field modeling and machine learning of electric-thermal-mechanical breakdown of polymer-based dielectrics. *Nat. Commun.* **10**, 1843 (2019).
31. Wu, C. et al. Rational design of all-organic flexible high-temperature polymer dielectrics. *Mater.* **5**, 2615–2623 (2022).
32. Wu, C. et al. Dielectric polymers tolerant to electric field and temperature extremes: integration of phenomenology, informatics, and experimental validation. *ACS Appl. Mater. Interfaces* **13**, 53416–53424 (2021).
33. Cheng, S. et al. Polymer dielectrics sandwiched by medium-dielectric-constant nanoscale deposition layers for high-temperature capacitive energy storage. *Energy Storage Mater.* **42**, 445–453 (2021).
34. Azizi, A. et al. High-performance polymers sandwiched with chemical vapor deposited hexagonal boron nitrides as scalable high-temperature dielectric materials. *Adv. Mater.* **29**, 1701864 (2017).
35. Dong, J. F. et al. Enhancing high-temperature capacitor performance of polymer nanocomposites by adjusting the energy level structure in the micro-/mesoscopic interface region. *Nano Energy* **99**, 107314 (2022).
36. Ren, W. B. et al. Scalable ultrathin all-organic polymer dielectric films for high-temperature capacitive energy storage. *Adv. Mater.* **34**, 2207421 (2022).
37. Otsuka, S., et al. PoLyInfo: polymer database for polymeric materials design. In *Proc. International Conference on Emerging Intelligent Data and Web Technologies*, 22–29 (IEEE, Piscataway, New Jersey, United States, 2011).
38. Huan, Tran et al. A comprehensive polymer dataset for accelerated property prediction and design. *Sci. Data* **3**, 160012 (2016).
39. Alamri, A. et al. Improving the rotational freedom of polyetherimide: enhancement of the dielectric properties of a commodity high-temperature polymer using a structural defect. *Chem. Mater.* **34**, 6553–6558 (2022).
40. Hafner, J. Ab-initio simulations of materials using VASP: density-functional theory and beyond. *J. Comput. Chem.* **29**, 2044–2078 (2008).
41. Hafner, J. Materials simulations using VASP - a quantum perspective to materials science. *Comput. Phys. Commun.* **177**, 6–13 (2007).
42. Stöhr, M., Troy Van, V. & Alexandre, T. Theory and practice of modeling van der Waals interactions in electronic-structure calculations. *Chem. Soc. Rev.* **48**, 4118–4154 (2019).
43. Deák, P. et al. Accurate defect levels obtained from the HSE06 range-separated hybrid functional. *Phys. Rev. B* **81**, 153203 (2010).

Acknowledgements

This work was supported by the National Natural Science Foundation of China grants 51922056 (Q.L.), 92166203 (Q.L.) and 51921005 (J.L.H.).

Author contributions

Q.L. conceived the idea. Q.L. and R.W. designed the experiments. R.W., J.F., M.C.Y., Z.Y.R. and J.L.L. carried out the experiments. Y.J.Z. and M.X.L. performed the simulations. Q.L., J.L.H., J.H. and R.W. analyzed the data. Q.L. and R.W. wrote the manuscript. All authors discussed the results and commented on the manuscript.

Competing interests

The authors declare no competing interests.

Additional information

Supplementary information The online version contains supplementary material available at <https://doi.org/10.1038/s41467-023-38145-w>.

Correspondence and requests for materials should be addressed to Qi Li.

Peer review information *Nature Communications* thanks Jun-Wei Zha and the other, anonymous, reviewers for their contribution to the peer review of this work. A peer review file is available.

Reprints and permissions information is available at <http://www.nature.com/reprints>

Publisher's note Springer Nature remains neutral with regard to jurisdictional claims in published maps and institutional affiliations.

Open Access This article is licensed under a Creative Commons Attribution 4.0 International License, which permits use, sharing, adaptation, distribution and reproduction in any medium or format, as long as you give appropriate credit to the original author(s) and the source, provide a link to the Creative Commons license, and indicate if changes were made. The images or other third party material in this article are included in the article's Creative Commons license, unless indicated otherwise in a credit line to the material. If material is not included in the article's Creative Commons license and your intended use is not permitted by statutory regulation or exceeds the permitted use, you will need to obtain permission directly from the copyright holder. To view a copy of this license, visit <http://creativecommons.org/licenses/by/4.0/>.

© The Author(s) 2023